New insight into Pt nucleation mechanism on Si surface during galvanic displacement deposition.

Rachela G. Milazzo[1], Stefania M. S. Privitera[1z], Silvia Scalese[1], Salvatore Mirabella[2], Corrado Bongiorno[1], Salvatore Lombardo[1], Emanuele Rimini[1,2]

[1] CNR-IMM Institute for the Microelectronics and Microsystems, Z. I. VIII Strada 4, Catania, I-95121, Italy;

[2] Department of Physics and Astronomy, v. S. Sofia 64, I-95123, Catania, Italy

[z] stefania.privitera@imm.cnr.it

Abstract

The Pt electroless deposition on silicon has been investigated by Rutherford Backscattering Spectrometry (RBS) and Electron Microscopy. Platinum nanoparticles nucleate and grow at the Si surface and the chronoamperometric response of the process has been determined from the RBS spectra. Nucleation is quite complex and it includes the generation of primary non- growing clusters, with size smaller than 2 nm. Larger particles result both from dynamic coalescence of primary particles and from single ion attachment processes and at higher immersion time they grow according to the classical diffusion limited model. The analyses with electron microscopy, then, have highlighted the peculiar nano-porous structure of particles resulting a mixed aggregative-diffusion limited growth.

Introduction

Metal nanoparticles are carefully investigated in many research areas thanks to their properties, remarkably different from that of their bulk counterpart since the small size enables quantum effects and changes in the electronic band structure. From a chemical point of view also, the large surface to volume ratio and the increased density of unsaturated bonds make them more reactive to certain molecules. For all these reasons

nanoparticles can be implemented in different fields and for a variety of applications, such as optoelectronics, medicals, drug delivery, sensors and healthcare [1], [2], [3], [4].

Excitation of the plasmonic nanoparticles at their resonant wavelength produces a collective coherent oscillation of conduction band electrons and an enhancement of the electric field at specific hotspots. At these hotspots, the plasmon excitation can decay and excites a single electron to create a highly-energetic electron–hole pair, the so called hot electrons, that can assist the catalytic reactions [5,6] otherwise hard to accomplish. A challenging goal for the future is to develop multifunctional materials able to perform catalytic synthesis at room temperature and under ambient conditions to prevent the degradation of the catalyst itself. Tuning of LSPR is the most promising strategy to control the injection of hot electrons. Among the different metal nanoparticles (NPs) those of platinum are of relevant interest. As an example, Pt NPs have found application in metal assisted chemical etching of silicon, a beneficial strategy to produce mesoporous silicon, a key material for several applications in optoelectronics, photovoltaic, batteries, supercapacitors and biochemistry sensors [7], [8], [9], [10], [11].

Moreover, platinum is the most widely used catalyst for many electrochemical applications, such as fuel cells or water splitting cells[12], [13],[14], [15] since, among the catalytically active metals, it is the most efficient for HER (Hydrogen Evolution Reaction) and it can remain stable in either an acidic or an alkaline electrolyte. Si surfaces via metal NPs improves the photo-electrochemical (PEC) characteristics of Si electrodes, such as their catalytic ability and stability , and therefore could make silicon a suitable choice for efficient conversion of solar energy to chemical fuels [16], [17–19].

It is therefore clear that the fabrication of Pt NPs with controlled sizes and shapes is an attractive goal and, among the deposition strategies, spontaneous galvanic displacement [20–22] takes advantage of the simplicity of the experimental apparatus and of the large variety of nanostructures that can be fabricated. Furthermore, particles are grown directly on a semi-conductive (Si, 3C-SiC, GaAs) or conductive substrate (Ni, Cu) ensuring also electrical connection. [23], [24], [25,26], [27].

In our previous works we have analyzed the electroless deposition of silver and gold on silicon substrates by Rutherford Backscattering Spectrometry (RBS)[28,29]. This technique allows the quantitative measure of the

deposited metallic atoms, without parasitic current due to substrate reactivity to the other species present in the solution. We have found that, for both silver and gold, clusters nucleation occurs instantaneously and the subsequent particle growth is governed by a diffusion limited mechanism. In the present work we analyze the Pt galvanic displacement deposition following the same approach. Coupling of the results obtained from RBS spectra with morphological characterization indicates that the nucleation process is quite complex and does not fit properly with the classical diffusion limited model[30], [31]. The nucleation will produce (i) classical particles that will grow by single atom attachment[31] and (ii) non-growing primary clusters that will merge to generate classical particles. High Resolution Transmission Electron Microscopy (HRTEM) analyses evidenced the unique crystalline arrangement of each cluster, showing a very peculiar nano-porous structure.

Experimental

The starting substrates were cut from Si(100) n-type wafers (P-doped with resistivity 3-5 Ω cm). Prior deposition, each sample was sonicated at 60°C with acetone and then dipped in 3M HF. Two sets of samples were prepared: one with etching time of 10s, another with 4min. On both the sets the Pt was electroless deposited using a solution containing 1mM Na_2PtCl_6 and 4.8M HF. The samples were dipped in the plating solution for different times, ranging from 10s to 16min. After deposition, each sample was rinsed in deionized water, to promote a quick removal of the reaction products, and then dried in air. All the procedures have been carried out at RT (20°C), with ambient lighting, in a ventilated cup.

For RBS measurements samples were analyzed using 2.0MeV He^+ ions scattered by target atoms at 165°. The energy of the scattered ions was detected by a solid-state surface barrier Si detector with 15keV resolution. The analyzed area of each sample was about 1mm². Spectra have been analyzed by RUMP[32] software, to obtain the areal density of Pt atoms and the thickness crossed by backscattered ions. The morphology of the particles has been investigated by Scanning Electron Microscopy (SEM) using a ZEISS SUPRATM 35 and in plan view TEM with a Jeol JEM 2010F Microscope. For the plan view TEM the as deposited samples have been treated according to the standard mechanical thinning procedure. The ion milling has been done with a PIPSII System by Gatan® with a starting beam energy of 1.5keV and a final polishing of 0.2keV but without N_2 cooling.

Results and Discussion

The deposition based on the galvanic displacement is spontaneous and it is driven by the overlap between redox potential of the metal/metal ions couple (in the solution) and the energy Fermi level on the semiconductor side[33]. The electron transfer may take place from (i) the conduction band, (ii) surface states or, as for noble metal deposition, from (iii) the valence band to the metal ions. The Si/Pt case is outlined in Figure 1**Errore. L'origine riferimento non è stata trovata.**. By considering a dopant concentration $N_D \approx 1.3 \times 10^{15}$ cm^{-3} at room temperature, the extrinsic Fermi level is located 0.28eV above the mid-gap of Si.
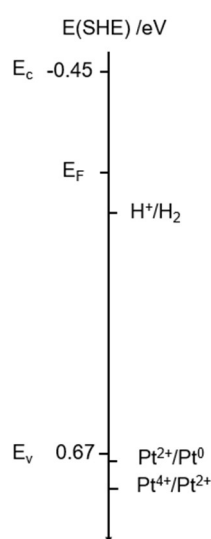

Figure 1 : A qualitative comparison between the electrochemical energy levels of Si and of the redox systems involved in the galvanic displacement deposition of Pt on a Si substrate.
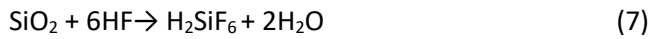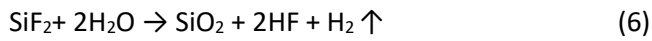
The deposition is based on the reduction of (PtCl6) $^{2-}$ to Pt^0 through four electrons transfer from the valence band of silicon (mechanism iii), with two consecutive steps[34]:

$(PtCl_6)^{2-} + 2e^- \rightarrow (PtCl_4)^{2-} + 2Cl^-$ V=0.75 V(SHE)   (1)

$(PtCl_4)^{2-} + 2e^- \rightarrow Pt + 4Cl^-$ V=0.68V(SHE)   (2)

There is a parallel reaction related to the dissolution of the oxidized silicon in the presence of fluoride species, the mechanism is complex and is related to electron transfer from the surface states to the electrolyte. However, it has been largely discussed in the literature and it is generally accepted that the reaction is accompanied by hydrogen generation and incorporation[35], [36] as a result the silicon surface shows increased roughness and nano-porosity at long time. Possible reactions are[37],[38],[39] :

$Si + 4HF + 4h^+ \rightarrow SiF_4 + 4H^+$ (3)

$SiF_4 + 2HF \rightarrow H_2SiF_6$ (4)

Or

$Si + 2HF + 2h^+ \rightarrow SiF_2 + 2H_+$ (5)

$SiF_2 + 2H_2O \rightarrow SiO_2 + 2HF + H_2 \uparrow$ (6)

$SiO_2 + 6HF \rightarrow H_2SiF_6 + 2H_2O$ (7)

The main difference between the two mechanisms lies in the holes number, 4 for $_{SiF4+2HF} \rightarrow H2SiF6$

(**4** and 2 for reaction $Si+2HF+2h+ \rightarrow SiF2+2H+$ (**5**, needed to etch a Si atom.

According to previous findings [40], both reactions occur and the number of holes ranges between 2 and 4.

It is commonly accepted that the limiting step for electroless deposition of noble metal on silicon is the diffusion of metal ions through the boundary layer to the silicon/electrolyte interface and the growth is driven by single ion attachment to the substrate or to the already generated metal nuclei [41–44]. According to the classical model, the deposition rate is very fast in the early stages, since the arising particles are far apart from each other and the corresponding diffusion regions are hemispherical (r_{3D}). In this regime the radius of each particle grows following Eq. 8:

$$r(t)_{3D} = (2V_m Dc)^{1/2} t^{1/2}$$

<div align="right">Eq. 8</div>

Being V_m the molar volume, c and D the concentration and diffusion coefficient of the ions in the bulk solution, respectively. At that time, nucleation of new particles is still allowed in the area outside of the diffusion regions. Gradually, the diffusion regions around particles start to overlap and the particles evolve from hemispherical to a planar shape (r_{2D}). Nucleation is thus hindered and the current decreases.

The growth rate in this case is given by

$$r(t)_{2D} = \left(\frac{2Dc\pi^{1/2}}{3V_m} \right)^{1/3} t^{1/6}$$

Eq. 9:

$$r(t)_{2D} = \left(\frac{2Dc\pi^{1/2}}{3V_m}\right)^{1/3} t^{1/6}$$

<div align="right">Eq. 9</div>

However this description has some limits since it does not take into account for the modification of the substrate during the reaction, the presence of HF in the plating solution, that interacts both with the substrate and the growing particles, [45][46][47] and assumes the nanoparticles are fixed on the hosting substrate.

a. Electron microscopy analyses

The plan view TEM micrographs of the sample dipped for 30s and 60s in the Pt deposition solution are shown in

Figure 2 and Figure 3 respectively. In both the samples two kinds of particles can be observed: circular, very small (with a radius lower than 1nm) nuclei, and large agglomerates. The radii distributions for the aforementioned particles are shown in the bar plot of the inset. The presence of very small particles, so called 'primary clusters', has been found to occur also upon electrodeposition or in the direct synthesis from Pt based solutions [48–54]. For both dipping times, the density, as calculated from the micrographs, is very high and amounts to 2.43×10^{12} cm^{-2} and 8×10^{10} cm^{-2}, respectively but they do not grow with time as summarized in Table 1. Such a behavior has been previously explained by analogy with a close shell structure with magic size or to stabilization of their outer surface by some chemical species of the solution[55]. The large nano-particles instead, referred as 'classical', exhibit a complex flower-like porous structure with several nano-crystalline regions. The SAED (Selected Area Electron Diffraction), reported as inset in Figure 3a, shows the <111> Pt rings, while Figure 3c displays the Moiré fringes, arising from superimposition of crystalline lattices[56]. The density of large particles does not change with deposition time, it amounts to 9×10^8 cm^{-2}, in contrast radii grow quickly, doubling in 30s. Such a behavior as well as their peculiar poly crystalline nature,

suggest that their growth occurs for both dynamic coalescence of primary clusters and impingement of ions to the growing nuclei.
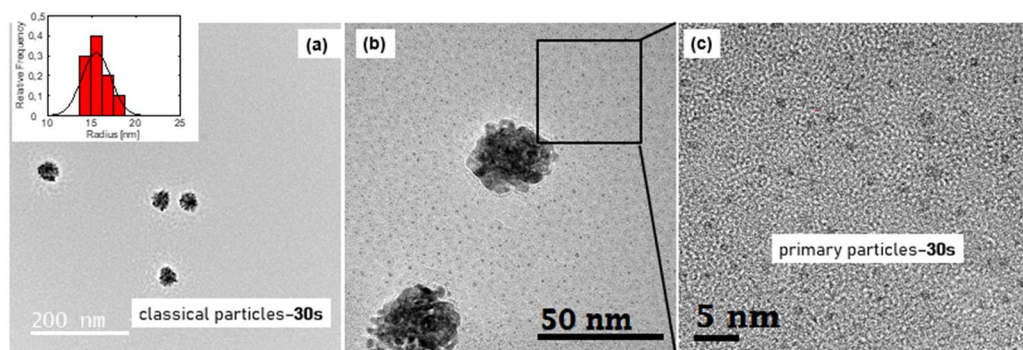

Figure 2: (a), (b) and (c) TEM plan view micrograph of the sample dipped in the deposition solution for 30s at increasing magnification showing the co presence of classical and primary PtNPs. The inset in (a) is the radii distribution for classical particles.
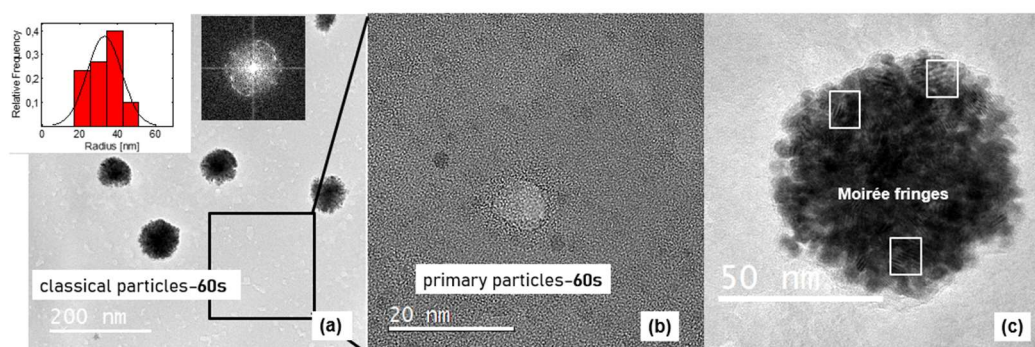

Figure 3 (a) TEM micrograph of Pt NPs on Si after 60s dipping in the plating solution, the insets are the radii bar plot and the SAED on the grain respectively; (b) Magnification of the region enclosed by the square in (a), showing the primary clusters and (c) TEM micrograph of another large Pt particle, showing Moirée fringes.

	classical particles		primary clusters	
	radius [nm]	NPs cm^{-2}	NPs cm^{-2}	radius [nm]
30s	15.6 ± 1.6	9.04×10^{8}	2.43×10^{12}	< 1
60s	33 ± 9	9.08×10^{8}	8×10^{10}	1-2

Table 1: A summary of the size and density found from TEM analyses in plan view for dipping time of 30s and 60s.

The samples obtained after longer deposition times have been analyzed by SEM and the radii distribution has been evaluated, as shown Figure 4. Values refer to classical particles since primary clusters disappear with longer deposition times, see S2.
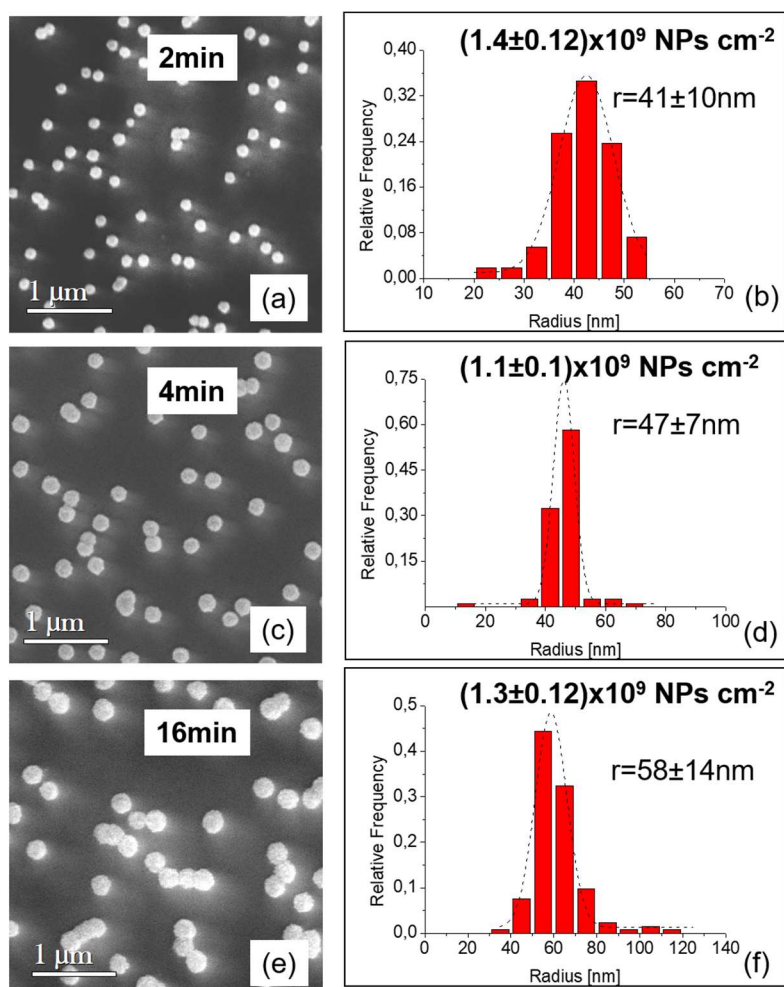

Figure 4: (a) SEM micrograph of the sample immersed for 2min; (c) 4min and (e) 16min. (b), (d) and (f) show the corresponding radii distributions as determined by SEM analysis.

The particle density does not change a lot since it amounts to 1.4×10^9 NPs cm^{-2} for 2min deposition time, 1.1×10^9 NPs cm^{-2} for 4min deposition time and 1.3×10^9 NPs cm^{-2} after an immersion time of 16min. The average radius increases from 41nm to 58nm by prolonging the dipping time from 2min to 16min. However while growing, closer particles may coalesce. In Figure 5 we report the data acquired for the radii of the

classical particles with increasing dipping time in the plating solution. In a Log Log scale the two models (Eq. 8 and

$$r(t)_{2D} = \left(\frac{2Dc\pi^{1/2}}{3V_m}\right)^{1/3} t^{1/6}$$

Eq. 9) correspond to two straight lines with slopes, α, of 0.5 and 0.16 respectively, being the growth rate faster (α≈0.5) when the diffusion regions are hemispherical. As seen in Figure 5, r does not show a constant variation with time. The slopes are reported in the same figure. The radii of particles obtained by deposition time from 30s to 120s exhibit a growth rate in disagreement with any expected trend being α >0.5. Again, such a behavior is consistent with the electrochemical aggregative growth mechanisms [52], [57]. For longer times, instead, primary clusters have already coalesced and the data are in agreement with the model of planar diffusion regions, with α= 0.2.
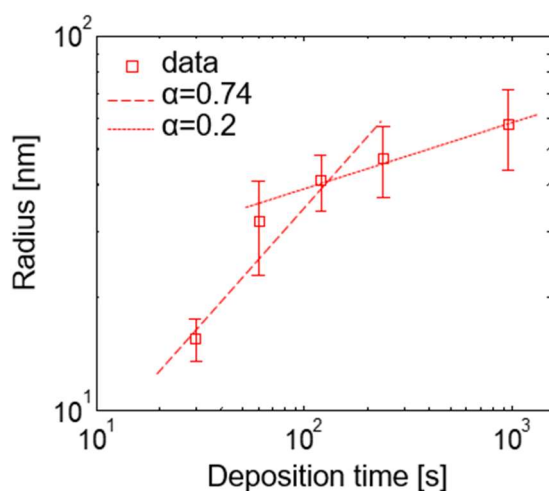

Figure 5: The Log Log scale of r(t) as measured by electron micrographs (bars are standard deviations).

(Results are quite different from those obtained for Ag and Au following the same experimental procedure [34, 35]. For 40s deposition time the fractional covered area for Ag was 0.28 [34], for Pt is instead very low, less than 2% as shown in fig. 1a and as determined by RBS analysis (see fig. 5). Ag nanoparticles also formed a well interconnected metal network, while those made of Pt are sparse and maintain an in-plan round shape.

Moreover, for Pt we did not observe any competing mechanism between the 3D or Island growth modes as that found for gold [37].)

b. RBS analyses

The RBS energy spectra associated to the helium ions backscattered from the deposited Pt atoms for different immersion times are reported in Figure 6.
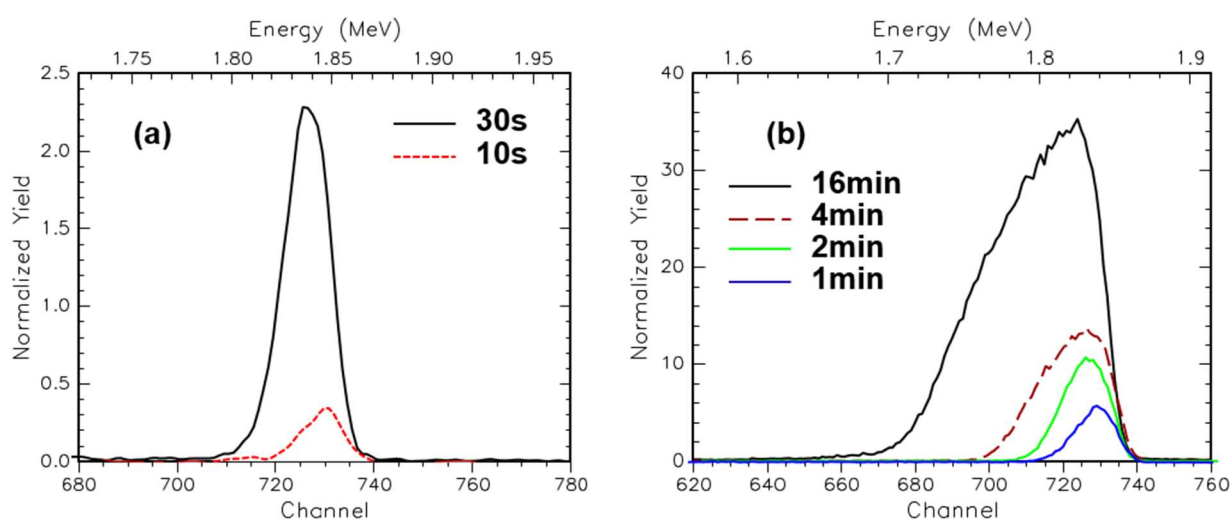

Figure 6 (a)-(b) RBS energy spectra of 2.0 MeV He+ ions backscattered from Pt atoms deposited on the Si substrate after immersion in the 1mM solution for the 10-960s time range;

There are a lot of works aiming to the modeling of RBS spectra with the sample surface, it is commonly accepted that an increasing roughness results in a lowering of the maximum yield and in a more pronounced spread of the energy distribution of backscattered ions[58]. Since the maximum yield resulting from a continuous thick film is higher than that coming from a partially covered surface, so by comparing the height of the experimental spectrum with that corresponding to a simulated continuous film it is possible to give the fractional covered area[59] (see Figure S1). The coating rate is very slow, as shown in Figure 7a: after a dipping for 10s in the solution, only 1% of the Si surface was covered with metal particles and even after 16min the covered area approaches 13%. The observed trend is indicative of a 3D Volmer-Weber growth mode [60]. The areal atomic density measured from RBS energy spectra, provides, by differentiation, the

chronoamperometric curve for the Pt deposition on silicon. The J(t) curve is reported in Figure 7 b. For the calculation we assumed that to reduce one Pt ion to the metallic state, four electrons are required. The deposition current amounts to a few $\mu A\ cm^{-2}$. In the case of gold, with the same deposition procedure, the current density was more than one order of magnitude higher. One reason could be the stability of $(PtCl_x)$ in the water [61] as well as the two steps reaction related to Pt ions reduction.

The current density, J, for Pt exhibits a very fast increase up to about 100s, then it decreases as expected for a diffusion limited growth. Data are modeled according to the Scharikfer Hills model [62] and for long times it follows

Eq. **10**, where c is the $(PtCl6)^{2+}$ ions concentration in the bulk of solution and D the their diffusion coefficient.

$$J(t) \approx nFc \sqrt{\frac{D}{\pi t}}$$

Eq. 10

Fitting to the experimental data, shown in Figure 7b, allows to determine a diffusion coefficient $D=2.5 \times 10^{-6}$ $cm^2\ s^{-1}$ in agreement with previous findings[63]. The final increase in the current density has been previously related to the occurrence of new nucleation events[36].
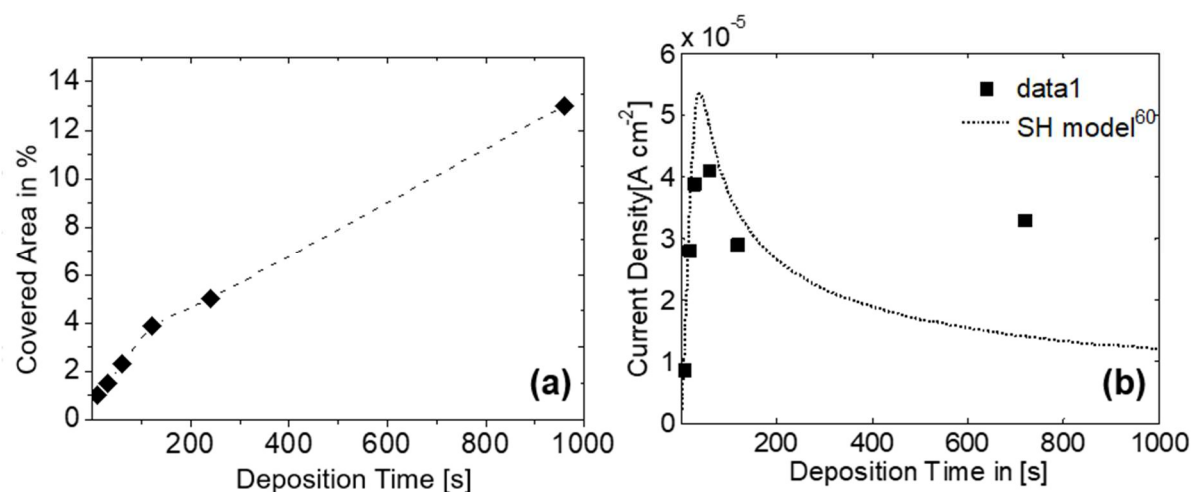

Figure 7 : RBS results, (a) % of the Si substrate surface covered by Pt, as computed by RBS spectra and (b) Current-Time curve for Pt electroless deposition on Si.

The RBS spectra have been also taken into account in the evaluation of primary clusters. Since the RBS signal is the energy distribution of the ions backscattered from the target[64], [65] the FWHM (Full Width at Half Maximum) gives the thickness, t crossed by the backscattered ions according to Eq. 11:

$\Delta E_{FWHM} = -(dE/dx)\, t$

Eq. 11

Where ΔE_{FWHM} is the energy spread taken at FWHM of each spectrum and dE/dx is stopping power of the material[66], [67] for Pt is 138.2 (eV Å^{-1}) [68].

The total yield of each spectrum has been split in 10 sub regions, as shown Figure 8 a, for each of them we computed with RUMP the corresponding areal density, A_i, while the thickness, t_i, crossed by backscattered ions, has been obtained from Eq. 11. If t_i is both the height and the radius of a cylindrical particle with volume V_i it is possible obtain the corresponding number N_i of clusters with size t_i from Eq. 12, being ρ_{Pt} the Pt atomic density, 6.61×10^{22} atoms cm^{-3}.

$$N_i[NPs\ cm^{-2}] = \frac{A_i}{V_i \rho_{Pt}}$$

Eq. 12

With such a count, we obtained comprehensive overview on both primary and classical particles: in Figure 8 b we show the bar plot for the sample dipped for 60s in the plating solution, reporting the number of clusters with a given t_i. There are more than 10^{10} particles cm^{-2} with t_i less than 10nm, while for the remaining, about 10^9 it ranges between 10 and 45nm (see for comparison the measured r, 33nm, from Table **1**, in good agreement with cylindrical approximation).
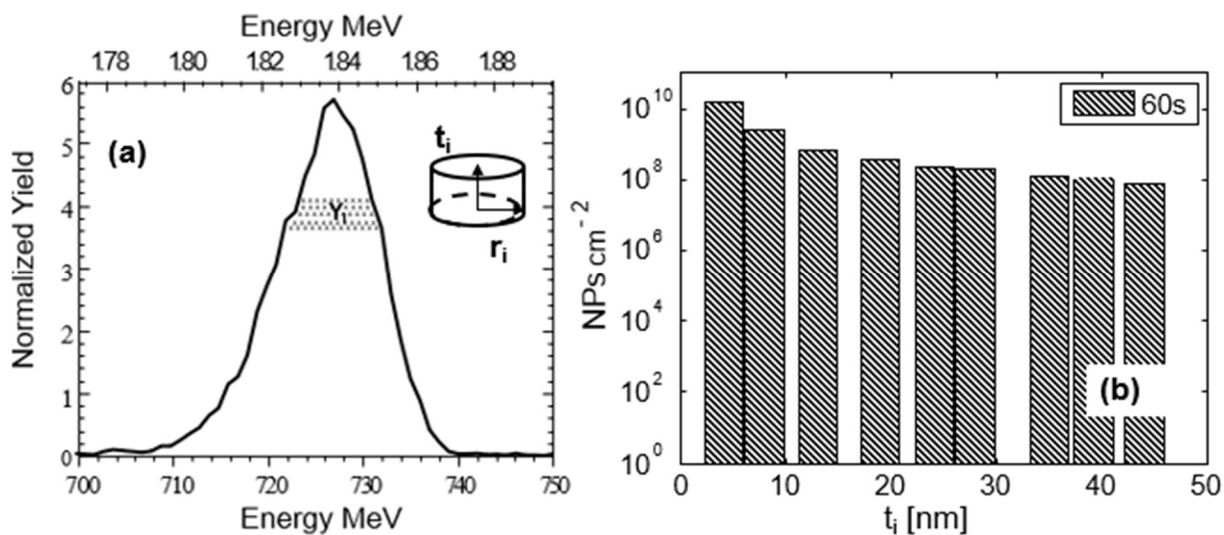
Figure 8: RBS analyses (a) an illustration of the split done on each spectrum, to calculate the thickness crossed by backscattered ions and (b).

(Un' altra possibilità per la figura 8 è questa e ci sarebbe da aggiungere al testo: In figure 8c we report the same data of b but for deposition time ranging from 10 to 120s. Results show that primary clusters density grows up to 30-60s then they convert in classical particles by aggregation. The sample dipped for 120s showed a full classical behavior.
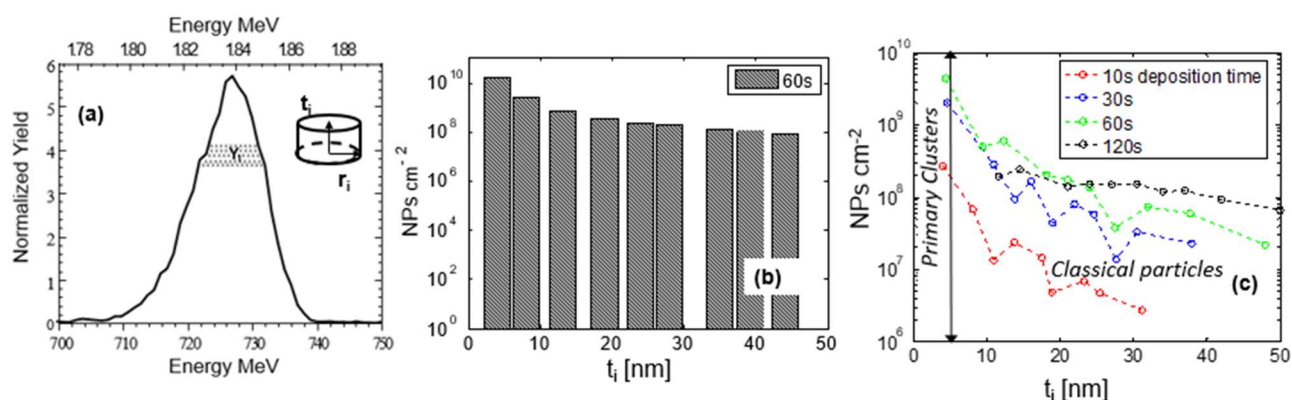

Figure 8 prova 2 : RBS analyses (a) an illustration of the split done on each spectrum, to calculate the thickness crossed by backscattered ions and (b), the same as for (b) but for several deposition times.)

Conclusions

The electroless Pt deposition on Si has been investigated with RBS analyses and electron microscopy. The analyses pointed out a very complex nucleation mechanism that include the generation of both primary clusters, with size below 2nm, and classical particles. The formers are stable, do not grow by direct attachment and their presence is not predicted by the classical theory. They can move on the silicon substrate supporting self-dynamic coalescence and once they have reached the proper size, they start to grow by direct attachment. They can also attach to the already present classical particles that will thus grow faster than expected. The occurrence of this mechanism is supported by the porous poly-crystalline texture of each particles as outlined by the high-resolution TEM and the RBS analyses.

References

(1)   Peiris, S.; McMurtrie, J.; Zhu, H. Y. Metal Nanoparticle Photocatalysts: Emerging Processes for Green Organic Synthesis. *Catal. Sci. Technol.* **2016**, *6* (2), 320–338. https://doi.org/10.1039/c5cy02048d.

(2)   Moores, A.; Goettmann, F. The Plasmon Band in Noble Metal Nanoparticles: An Introduction to Theory and Applications. *New Journal of Chemistry*. The Royal Society of Chemistry July 31, 2006, pp 1121–1132. https://doi.org/10.1039/b604038c.

(3)   Willets, K. A.; Van Duyne, R. P. Localized Surface Plasmon Resonance Spectroscopy and Sensing. *Annu. Rev. Phys. Chem.* **2007**, *58* (1), 267–297. https://doi.org/10.1146/annurev.physchem.58.032806.104607.

(4)   Mie, G. Beiträge Zur Optik Trüber Medien, Speziell Kolloidaler Metallösungen. *Ann. Phys.* **1908**, *330* (3), 377–445. https://doi.org/10.1002/andp.19083300302.

(5)   Nedrygailov, I. I.; Moon, S. Y.; Park, J. Y. Hot Electron-Driven Electrocatalytic Hydrogen Evolution Reaction on Metal–Semiconductor Nanodiode Electrodes. *Sci. Rep.* **2019**, *9* (1), 1–9. https://doi.org/10.1038/s41598-019-42566-3.

(6)   Kontoleta, E.; Askes, S. H. C.; Garnett, E. C. Self-Optimized Catalysts: Hot-Electron Driven Photosynthesis of Catalytic Photocathodes. *ACS Appl. Mater. Interfaces* **2019**, *11* (39), 35713–35719. https://doi.org/10.1021/acsami.9b10913.

(7)   Ahmad, M. Z.; Akhter, S.; Jain, G. K.; Rahman, M.; Pathan, S. A.; Ahmad, F. J.; Khar, R. K. Metallic

        Nanoparticles: Technology Overview and Drug Delivery Applications in Oncology. *Expert Opinion on*

        Drug Delivery. Taylor & Francis August 2010, pp 927–942.

        https://doi.org/10.1517/17425247.2010.498473.

(8)   Yae, S.; Morii, Y.; Fukumuro, N.; Matsuda, H. Catalytic Activity of Noble Metals for Metal-Assisted

        Chemical Etching of Silicon. *Nanoscale Res. Lett.* **2012**, *7* (1), 352. https://doi.org/10.1186/1556-

        276X-7-352.

(9)   Kolasinski, K. W. Silicon Nanostructures from Electroless Electrochemical Etching. *Curr. Opin. Solid*

        State Mater. Sci. **2005**, *9* (1–2), 73–83. https://doi.org/10.1016/j.cossms.2006.03.004.

(10)   Milazzo, R. G.; D'Arrigo, G.; Spinella, C.; Grimaldi, M. G.; Rimini, E. Ag-Assisted Chemical Etching of

        (100) and (111) n-Type Silicon Substrates by Varying the Amount of Deposited Metal. *J. Electrochem.*

        Soc. **2012**, *159* (9), D521–D525. https://doi.org/10.1149/2.008209jes.

(11)   Cristoforetti, G.; Londrillo, P.; Singh, P. K.; Baffigi, F.; D'Arrigo, G.; Lad, A. D.; Milazzo, R. G.; Adak, A.;

        Shaikh, M.; Sarkar, D.; Chatterjee, G.; Jha, J.; Krishnamurthy, M.; Kumar, G. R.; Gizzi, L. A. Transition

        from Coherent to Stochastic Electron Heating in Ultrashort Relativistic Laser Interaction with

        Structured Targets. *Sci. Rep.* **2017**, *7* (1). https://doi.org/10.1038/s41598-017-01677-5.

(12)   Lindgren, P.; Kastlunger, G.; Peterson, A. A. A Challenge to the G ~0 Interpretation of Hydrogen

        Evolution. *ACS Catal.* **2020**, *10* (1), 121–128. https://doi.org/10.1021/acscatal.9b02799.

(13)   Milazzo, R. G.; Privitera, S. M. S.; D'Angelo, D.; Scalese, S.; Di Franco, S.; Maita, F.; Lombardo, S.

        Spontaneous Galvanic Displacement of Pt Nanostructures on Nickel Foam: Synthesis,

        Characterization and Use for Hydrogen Evolution Reaction. *Int. J. Hydrogen Energy* **2018**.

        https://doi.org/10.1016/j.ijhydene.2018.03.042.

(14)   Wang, C.; Yin, L.; Zhang, L.; Liu, N.; Lun, N.; Qi, Y. Platinum-Nanoparticle-Modified TiO2 Nanowires

        with Enhanced Photocatalytic Property. *ACS Appl. Mater. Interfaces* **2010**, *2* (11), 3373–3377.

        https://doi.org/10.1021/am100834x.

(15)   Di Mauro, A.; Zimbone, M.; Scuderi, M.; Nicotra, G.; Fragalà, M. E.; Impellizzeri, G. Effect of Pt

Nanoparticles on the Photocatalytic Activity of ZnO Nanofibers. *Nanoscale Res. Lett.* **2015**, *10* (1), 1–7. https://doi.org/10.1186/s11671-015-1126-6.

(16)   Dai, P.; Xie, J.; Mayer, M. T.; Yang, X.; Zhan, J.; Wang, D. Solar Hydrogen Generation by Silicon Nanowires Modified with Platinum Nanoparticle Catalysts by Atomic Layer Deposition. *Angew. Chemie Int. Ed.* **2013**, *52* (42), 11119–11123. https://doi.org/10.1002/anie.201303813.

(17)   Fabre, B.; Li, G.; Gouttefangeas, F.; Joanny, L.; Loget, G. Tuning the Photoelectrocatalytic Hydrogen Evolution of Pt-Decorated Silicon Photocathodes by the Temperature and Time of Electroless Pt Deposition. *Langmuir* **2016**, *32* (45), 11728–11735. https://doi.org/10.1021/acs.langmuir.6b02122.

(18)   Sun, K.; Shen, S.; Liang, Y.; Burrows, P. E.; Mao, S. S.; Wang, D. Enabling Silicon for Solar-Fuel Production. *Chemical Reviews*. American Chemical Society September 10, 2014, pp 8662–8719. https://doi.org/10.1021/cr300459q.

(19)   Oh, I.; Kye, J.; Hwang, S. Enhanced Photoelectrochemical Hydrogen Production from Silicon Nanowire Array Photocathode. *Nano Lett.* **2012**, *12* (1), 298–302. https://doi.org/10.1021/nl203564s.

(20)   Alia, S. M.; Yan, Y. S.; Pivovar, B. S. Galvanic Displacement as a Route to Highly Active and Durable Extended Surface Electrocatalysts. *Catalysis Science and Technology*. Royal Society of Chemistry October 1, 2014, pp 3589–3600. https://doi.org/10.1039/c4cy00736k.

(21)   Carraro, C.; Maboudian, R.; Magagnin, L. Metallization and Nanostructuring of Semiconductor Surfaces by Galvanic Displacement Processes. *Surface Science Reports*. North-Holland December 31, 2007, pp 499–525. https://doi.org/10.1016/j.surfrep.2007.08.002.

(22)   Tang, J.; Ou, Q.; Zhou, H.; Qi, L.; Man, S. Seed-Mediated Electroless Deposition of Gold Nanoparticles for Highly Uniform and Efficient SERS Enhancement. *Nanomaterials* **2019**, *9* (2), 185. https://doi.org/10.3390/nano9020185.

(23)   Han, T.; Privitera, S.; Milazzo, R. G.; Bongiorno, C.; Di Franco, S.; La Via, F.; Song, X.; Shi, Y.; Lanza, M.; Lombardo, S. Photo-Electrochemical Water Splitting in Silicon Based Photocathodes Enhanced by Plasmonic/Catalytic Nanostructures. *Mater. Sci. Eng. B Solid-State Mater. Adv. Technol.* **2017**, *225*.

https://doi.org/10.1016/j.mseb.2017.08.022.

(24) Milazzo, R. G.; Privitera, S.; Litrico, G.; Scalese, S.; Mirabella, S.; La Via, F.; Lombardo, S.; Rimini, E.

Formation, Morphology, and Optical Properties of Electroless Deposited Gold Nanoparticles on 3C-

SiC. *J. Phys. Chem. C* **2017**, *121* (8). https://doi.org/10.1021/acs.jpcc.6b11638.

(25) Gaikwad, R.; Djokić, S. S.; Thundat, T. Galvanic Deposition of Gold on GaAs: A Tip-Induced

Lithography Approach. *J. Electrochem. Soc.* **2015**, *162* (9), D486–D489.

https://doi.org/10.1149/2.1001509jes.

(26) Hormozi Nezhad, M. R.; Aizawa, M.; Porter, L. A.; Ribbe, A. E.; Buriak, J. M. Synthesis and Patterning

of Gold Nanostructures on InP and GaAs via Galvanic Displacement. *Small* **2005**, *1* (11), 1076–1081.

https://doi.org/10.1002/smll.200500121.

(27) Lahiri, A.; Pulletikurthi, G.; Endres, F. A Review on the Electroless Deposition of Functional Materials

in Ionic Liquids for Batteries and Catalysis   . *Frontiers in Chemistry* . 2019, p 85.

(28) Milazzo, R. G.; Mio, A. M.; D'Arrigo, G.; Spinella, C.; Grimaldi, M. G.; Rimini, E. Electroless Deposition

of Gold Investigated with Rutherford Backscattering and Electron Microscopy. *2014 IEEE 9th*

Nanotechnol. Mater. Devices Conf. **2014**, 37–40. https://doi.org/10.1109/NMDC.2014.6997416.

(29) Milazzo, R. G.; D'Arrigo, G.; Mio, A. M.; Spinella, C.; Grimaldi, M. G.; Rimini, E. Electroless Deposition

of Silver Investigated with Rutherford Backscattering and Electron Microscopy. *ECS J. Solid State Sci.*

Technol. **2014**, *3* (7), P235–P242. https://doi.org/10.1149/2.0031407jss.

(30) Hyde, M. E.; Compton, R. G. A Review of the Analysis of Multiple Nucleation with Diffusion

Controlled Growth. *Journal of Electroanalytical Chemistry*. Elsevier June 5, 2003, pp 1–12.

https://doi.org/10.1016/S0022-0728(03)00250-X.

(31) Scharifker, B. *THEORETICAL AND EXPERIMENTAL STUDIES OF MULTIPLE NUCLEATION*.

(32) Climent-Font, A.; Wätjen, U.; Bax, H. Quantitative RBS Analysis Using RUMP. On the Accuracy of the

He Stopping in Si. *Nucl. Inst. Methods Phys. Res. B* **1992**, *71* (1), 81–86.

https://doi.org/10.1016/0168-583X(92)95343-P.

(33) Peng, K.; Lu, A.; Zhang, R.; Lee, S.-T. Motility of Metal Nanoparticles in Silicon and Induced

Anisotropic Silicon Etching. *Adv. Funct. Mater.* **2008**, *18* (19), 3026–3035.

https://doi.org/10.1002/adfm.200800371.

(34)   Hughes, R. Https://Issuu.Com/Time-to-Wake-up/Docs/Electrochemical_redox_potential. *Journal of Chemical Information and Modeling*. 2008, p 287. https://doi.org/10.1017/CBO9781107415324.004.

(35)   Allongue, P.; Henry De Villeneuve, C.; Pinsard, L.; Bernard, M. C. Evidence for Hydrogen Incorporation during Porous Silicon Formation(1) Allongue, P.; Henry De Villeneuve, C.; Pinsard, L.; Bernard, M. C. Evidence for Hydrogen Incorporation during Porous Silicon Formation. Appl. Phys. Lett. 1995, 67, 941. Https://Doi.Org. *Appl. Phys. Lett.* **1995**, *67*, 941. https://doi.org/10.1063/1.114702.

(36)   Lombardi, I.; Marchionna, S.; Zangad, G.; Pizzini, S. Effect of Pt Particle Size and Distribution on Photoelectrochemical Hydrogen Evolution by P-Si Photocathodes. *Langmuir* **2007**, *23* (24), 12413–12420. https://doi.org/10.1021/la7016165.

(37)   Peng, K.; Fang, H.; Hu, J.; Wu, Y.; Zhu, J.; Yan, Y.; Lee, S. T. Metal-Particle-Induced, Highly Localized Site-Specific Etching of Si and Formation of Single-Crystalline Si Nanowires in Aqueous Fluoride Solution. *Chem. - A Eur. J.* **2006**, *12* (30), 7942–7947. https://doi.org/10.1002/chem.200600032.

(38)   Lai, C. Q.; Zheng, W.; Choi, W. K.; Thompson, C. V. Metal Assisted Anodic Etching of Silicon. *Nanoscale* **2015**, *7* (25), 11123–11134. https://doi.org/10.1039/c5nr01916h.

(39)   Chartier, C.; Bastide, S.; Lévy-Clément, C. Metal-Assisted Chemical Etching of Silicon in HF-H2O2. *Electrochim. Acta* **2008**, *53* (17), 5509–5516. https://doi.org/10.1016/j.electacta.2008.03.009.

(40)   Xia, X. H.; Ashruf, C. M. A.; French, P. J.; Kelly, J. J. Galvanic Cell Formation in Silicon/Metal Contacts: The Effect on Silicon Surface Morphology. *Chem. Mater.* **2000**, *12* (6), 1671–1678. https://doi.org/10.1021/cm9912066.

(41)   Isaev, V. A.; Grishenkova, O. V.; Zaykov, Y. P. On the Theory of 3D Multiple Nucleation with Kinetic Controlled Growth. *J. Electroanal. Chem.* **2018**, *818*, 265–269. https://doi.org/10.1016/j.jelechem.2018.04.051.

(42)   Tomellini, M. Spatial Distribution of Nuclei in Progressive Nucleation: Modeling and Application.

Phys. A Stat. Mech. its Appl. **2018**, *496*, 481–494. https://doi.org/10.1016/j.physa.2017.12.150.

(43) Heerman, L.; Matthijs, E.; Langerock, S. The Concept of Planar Diffusion Zones. Theory of the

Potentiostatic Transient for Multiple Nucleation on Active Sites with Diffusion-Controlled Growth.

Electrochim. Acta **2001**, *47* (6), 905–911. https://doi.org/10.1016/S0013-4686(01)00792-7.

(44) Liu, H.; Penner, R. M. Size-Selective Electrodeposition of Mesoscale Metal Particles in the Uncoupled

Limit. *J. Phys. Chem. B* **2000**, *104* (39), 9131–9139. https://doi.org/10.1021/jp0017902.

(45) Milazzo, R. G.; Mio, A. M.; D'Arrigo, G.; Grimaldi, M. G.; Spinella, C.; Rimini, E. Coalescence of Silver

Clusters by Immersion in Diluted HF Solution. *J. Chem. Phys.* **2015**, *143* (2), 024306.

https://doi.org/10.1063/1.4926530.

(46) Milazzo, R. G.; Mio, A. M.; D'Arrigo, G.; Smecca, E.; Alberti, A.; Fisichella, G.; Giannazzo, F.; Spinella,

C.; Rimini, E. Influence of Hydrofluoric Acid Treatment on Electroless Deposition of Au Clusters.

Beilstein J. Nanotechnol. **2017**, *8*, 183–189. https://doi.org/10.3762/bjnano.8.19.

(47) Radisic, A.; Ross, F. M.; Searson, P. C. In Situ Study of the Growth Kinetics of Individual Island

Electrodeposition of Copper. **2006**. https://doi.org/10.1021/jp057549a.

(48) Imaoka, T.; Akanuma, Y.; Haruta, N.; Tsuchiya, S.; Ishihara, K.; Okayasu, T.; Chun, W. J.; Takahashi,

M.; Yamamoto, K. Platinum Clusters with Precise Numbers of Atoms for Preparative-Scale Catalysis.

Nat. Commun. **2017**, *8* (1), 1–8. https://doi.org/10.1038/s41467-017-00800-4.

(49) Sebetci, A.; Güvenç, Z. B.; Kökten, H. Thermodynamics of Small Platinum Clusters. In *Computational

Materials Science*; Elsevier, 2006; Vol. 35, pp 192–197.

https://doi.org/10.1016/j.commatsci.2004.08.016.

(50) Wei, H.; Huang, K.; Wang, D.; Zhang, R.; Ge, B.; Ma, J.; Wen, B.; Zhang, S.; Li, Q.; Lei, M.; Zhang, C.;

Irawan, J.; Liu, L. M.; Wu, H. Iced Photochemical Reduction to Synthesize Atomically Dispersed

Metals by Suppressing Nanocrystal Growth. *Nat. Commun.* **2017**, *8* (1).

https://doi.org/10.1038/s41467-017-01521-4.

(51) Abu-Thabit, N.; Makhlouf, A. S. H. Recent Approaches for Designing Nanomaterials-Based Coatings

for Corrosion Protection. In *Handbook of Nanoelectrochemistry: Electrochemical Synthesis Methods,*

Properties, and Characterization Techniques; Springer International Publishing, 2016; pp 309–332. https://doi.org/10.1007/978-3-319-15266-0_10.

(52) Ustarroz, J.; Altantzis, T.; Hammons, J. A.; Hubin, A.; Bals, S.; Terryn, H. The Role of Nanocluster Aggregation, Coalescence, and Recrystallization in the Electrochemical Deposition of Platinum Nanostructures. *Chem. Mater.* **2014**, *26* (7), 2396–2406. https://doi.org/10.1021/cm403178b.

(53) Mamme, M. H.; Köhn, C.; Deconinck, J.; Ustarroz, J. Numerical Insights into the Early Stages of Nanoscale Electrodeposition: Nanocluster Surface Diffusion and Aggregative Growth. *Nanoscale* **2018**, *10* (15), 7194–7209. https://doi.org/10.1039/c7nr08529j.

(54) Ustarroz, J.; Hubin, A.; Terryn, H. New Insights in Nanoelectrodeposition: An Electrochemical Aggregative Growth Mechanism BT - Handbook of Nanoelectrochemistry: Electrochemical Synthesis Methods, Properties, and Characterization Techniques; Aliofkhazraei, M., Makhlouf, A. S. H., Eds.; Springer International Publishing: Cham, 2016; pp 1349–1377. https://doi.org/10.1007/978-3-319-15266-0_10.

(55) Takesue, M.; Tomura, T.; Yamada, M.; Hata, K.; Kuwamoto, S.; Yonezawa, T. Size of Elementary Clusters and Process Period in Silver Nanoparticle Formation. *J. Am. Chem. Soc.* **2011**, *133* (36), 14164–14167. https://doi.org/10.1021/ja202815y.

(56) Williams, D. B.; Carter, C. B. *Transmission Electron Microscopy: A Textbook for Materials Science*; Springer US, 2009. https://doi.org/10.1007/978-0-387-76501-3.

(57) Ustarroz, J.; Hammons, J. A.; Altantzis, T.; Hubin, A.; Bals, S.; Terryn, H. A Generalized Electrochemical Aggregative Growth Mechanism. **2013**. https://doi.org/10.1021/ja402598k.

(58) Malinský, P.; Siegel, J.; Hnatowicz, V.; Macková, A.; Švorčík, V. Simulation of RBS Spectra with Known 3D Sample Surface Roughness. *Nucl. Instruments Methods Phys. Res. Sect. B Beam Interact. with Mater. Atoms* **2017**, *406*, 99–103. https://doi.org/10.1016/j.nimb.2017.02.020.

(59) Schneidewind, H.; Schüler, T.; Strelau, K. K.; Weber, K.; Cialla, D.; Diegel, M.; Mattheis, R.; Berger, A.; Möller, R.; Popp, J. The Morphology of Silver Nanoparticles Prepared by Enzyme-Induced Reduction. *Beilstein J. Nanotechnol.* **2012**, *3* (1), 404–414. https://doi.org/10.3762/bjnano.3.47.

(60)   Sayed, S. Y.; Wang, F.; Malac, M.; Meldrum, A.; Egerton, R. F.; Buriak, J. M. Heteroepitaxial Growth of Gold Nanostructures on Silicon by Galvanic Displacement. *ACS Nano* **2009**, *3* (9), 2809–2817. https://doi.org/10.1021/nn900685a.

(61)   Harada, M.; Einaga, H. Formation Mechanism of Pt Particles by Photoreduction of Pt Ions in Polymer Solutions. *Langmuir* **2006**, *22* (5), 2371–2377. https://doi.org/10.1021/la052378m.

(62)   Gunawardena, G.; Hills, G.; Montenegro, I.; Scharifker, B. Electrochemical Nucleation. Part I. General Considerations. *J. Electroanal. Chem.* **1982**, *138* (2), 225–239. https://doi.org/10.1016/0022-0728(82)85080-8.

(63)   Harada, M.; Okamoto, K.; Terazima, M. Diffusion of Platinum Ions and Platinum Nanoparticles during Photoreduction Processes Using the Transient Grating Method. *Langmuir* **2006**, *22* (22), 9142–9149. https://doi.org/10.1021/la061663i.

(64)   Mayer, M. *Rutherford Backscattering Spectrometry (RBS)*; 2003.

(65)   Ziegler, J. F.; Biersack, J. P. The Stopping and Range of Ions in Matter. In *Treatise on Heavy-Ion Science*; Springer US, 1985; pp 93–129. https://doi.org/10.1007/978-1-4615-8103-1_3.

(66)   Tabacniks, M. H. *A3-Rutherford Backscattering Spectrometry-RBS*.

(67)   Bauer ', P.; Steinbauer, E.; Biersack ' ', J. P. *The Width of an RBS Spectrum: Influence of Plural and Multiple Scattering*; 1992; Vol. 64.

(68)   Ziegler, J. F. *The Stopping and Range of Ions in Solids / J.F. Ziegler, J.P. Biersack, U. Littmark*; Littmark, U., Biersack, J. P., Eds.; Pergamon: New York, 1985.